CHEMISTRY OF MATERIALS

Article

pubs.acs.org/cm

Investigation of the Optical and Excitonic Properties of the Visible Light-Driven Photocatalytic $BiVO_4$ Material

Tilak Das,[†] Xavier Rocquefelte,*[,†,‡] Robert Laskowski,[§] Luc Lajaunie,[†,∥] Stéphane Jobic,[†] Peter Blaha,[⊥] and Karlheinz Schwarz[⊥]

[†]Institut des Matériaux Jean Rouxel, Université de Nantes, CNRS, Boîte Postale 32229, 44322 Nantes Cedex 3, France

[‡]Institut des Sciences Chimiques de Rennes, UMR 6226 CNRS, Université de Rennes 1, 35042 Rennes Cedex, France

[§]Institute of High Performance Computing, 1 Fusionopolis Way, #16-16 Connexis North, Singapore 138632

[∥]Laboratorio de Microscopías Avanzadas, Instituto de Nanociencia de Aragón, Universidad de Zaragoza, 50018 Zaragoza, Spain

[⊥]Institute of Materials Chemistry, Vienna University of Technology, Getreidemarkt 9/165-TC, A-1060 Vienna, Austria

Supporting Information

ABSTRACT: An investigation of the optical and excitonic properties of photocatalytic compounds based on both experimental and theoretical approaches is proposed. More specifically, this paper reports, for the first time, the local-field, optical anisotropy, and excitonic effects in $BiVO_4$, an active photocatalytic material in the visible range. The analyses are based on electron energy-loss spectroscopy measurements, ground-state density functional theory calculations, including crystal local-field effects, and many-body corrections using the Bethe–Salpeter equation. These results are supported by a comparison with two materials, namely, TiO_2 anatase and rutile, which are well-known to differ in their photocatalytic properties, those being important and negligible, respectively. The analogies found for these two categories of compounds allow the proposal of criteria that appear to be essential for producing an optimal photocatalytic material.

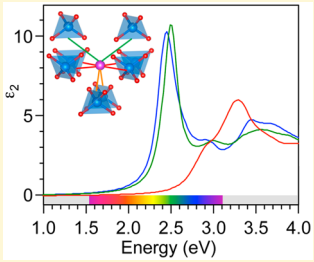

INTRODUCTION

In 1972, Honda and Fujishima first discovered that it was possible to promote the water splitting reaction, i.e., the decomposition of water into oxygen and hydrogen, by using an electrochemical device based on a TiO_2 anode and a platinum counter electrode exposed to ultraviolet (UV) light.[1] Over the past four decades, an important number of investigations have been devoted to such photoelectrochemical (PEC) reactions. Namely, TiO_2 is well-suited for photocatalytic applications because of its low cost, its high stability in aqueous solutions, and the right positioning of its valence band maximum (VBM) and conduction band minimum (CBM). Unfortunately, because of its overly large band gap (>3 eV), it operates only in the UV range and thus considerably decreases the efficiency of the conversion of solar energy to hydrogen. To have efficiencies of >15%, a band gap of <2.2 eV is required.[2] One strategy for reaching this band gap requirement is to consider multiternary oxides combining nd^0 (e.g., Ti^{4+}, V^{5+}, and Nb^{5+}) and ns^2 cations (e.g., Bi^{3+} or Sn^{2+}). Then, energy levels can be interspaced between the former valence and conduction bands and thus favor the absorption in the visible range. In that context, bismuth vanadate ($BiVO_4$), initially known for its ferroelastic and ionic conductivity properties,[3−5] is now considered as one of the most promising candidates for solar energy-to-hydrogen conversion processes operating in the visible light range.[6−8] However, its properties strongly depend on the allotropic form of $BiVO_4$. Three main polymorphs are known, namely, the zircon structure with tetragonal symmetry (Z_T-$BiVO_4$) and two (almost identical) scheelite structures with monoclinic (S_M-$BiVO_4$) and tetragonal (S_T-$BiVO_4$) symmetries, the former being ferroelastic and the latter paraelastic.[9] S_M- and S_T-$BiVO_4$ were selectively prepared by many groups, showing that S_M-$BiVO_4$ exhibits high photoelectrochemical (PEC) properties, whereas the photoactivity of Z_T-$BiVO_4$ is negligible.[6,7,9] It has also been demonstrated that both S_M- and S_T-$BiVO_4$ structures are photocatalytically active for the degradation of rhodamine B in solution under visible light, but not Z_T-$BiVO_4$.[10]

Recently, Fan et al.[11] shed light on the higher PEC activity of S_M-$BiVO_4$ compared to that of Z_T-$BiVO_4$. On the basis of surface photovoltage and transient photovoltage measurements under visible light irradiation, the authors clearly evidenced that photoinduced electrons (holes) flow from the surface (bulk) to the bulk (surface) for Z_T-$BiVO_4$ while the opposite is observed for S_M-$BiVO_4$. This explains why S_M-$BiVO_4$ is more active than Z_T-$BiVO_4$ for oxidation reactions. In addition, Li et al.[12] have shown that, under photoirradiation, efficient charge separation is achieved in S_M-$BiVO_4$, leading to a reduction reaction with photogenerated electrons and an oxidation reaction with photogenerated holes on the {010} and {110} crystal facets, respectively.

Received: June 5, 2016
Revised: March 28, 2017
Published: March 28, 2017

DOI: 10.1021/acs.chemmater.6b02261
Chem. Mater. 2017, 29, 3380−3386

To address the differences among S_M-, S_T-, and Z_T-$BiVO_4$, their optical properties have been investigated. To date, only the optical band gaps of S_M-, S_T-, and Z_T-$BiVO_4$ have been estimated on the basis of diffuse reflectance spectra of powder samples, and no experimental investigation of their frequency-dependent dielectric function (DF) has been reported. From the theoretical side, a significant number of studies habe been performed using density functional theory (DFT) with the generalized gradient approximation (GGA) and hybrid functionals. However, contradictory results have been published. For instance, the band gap nature of S_M-$BiVO_4$ was reported as both direct[2,13] and indirect.[14,15] Moreover, two different groups have reported simulations of the frequency-dependent dielectric function,[14,15] suggesting that the optical anisotropy is strong in S_M-$BiVO_4$ and negligible in Z_T-$BiVO_4$.[14]

Clearly, all these previous studies of the optical properties of $BiVO_4$ suffer from being purely experimental or theoretical. An investigation of the optical and excitonic properties of $BiVO_4$ combining experiments and theory to improve our understanding of the photocatalytic activity of this material is still missing. This is, indeed, the main purpose of this work, which reports, for the first time, on the local-field, optical anisotropy, and excitonic effects in S_M- and Z_T-$BiVO_4$, based on electron energy-loss spectroscopy (EELS) measurements, ground-state DFT calculations, including crystal local-field effects[16] (LFE), and many-body corrections using the Bethe−Salpeter equation[17] (BSE). Excellent agreement is obtained between EELS experiments and DFT calculations, which fully validates such *ab initio* calculations as a starting point for more sophisticated calculations devoted to the excitonic properties. In particular, solving the BSE allows one to study the spatial distribution of the photoinduced electron−hole pairs, i.e., the excitons, in S_M- and Z_T-$BiVO_4$ phases, and evidences the impact of the long-range crystalline structure on it. From this work, a unified picture of the optical and excitonic properties of S_M- and Z_T-$BiVO_4$ that emphasizes the link among the nature of the band gap, the photocatalytic activity, and the excitonic properties is proposed. Finally, this result is supported by a comparison of two materials, namely, TiO_2 anatase and rutile, which are well-known for the differences in their photocatalytic properties, being important and negligible, respectively.

RESULTS AND DISCUSSION

In structural terms, S_M- and S_T-$BiVO_4$ are very similar,[18] except for a small distortion, which reduces the symmetry from tetragonal (space group $I4_1/a$ for S_T, with $a = b = 5.147$ Å and $c = 11.7216$ Å) to monoclinic (space group $I2/b$ for S_M, with $a = 5.1935$ Å, $b = 5.0898$ Å, and $c = 11.6972$ Å). In contrast, the zircon phase[19] (Z_T-$BiVO_4$, space group $I4_1/amd$, with $a = b = 7.303$ Å and $c = 6.584$ Å) is significantly different from the two scheelite phases, leading to a large volume expansion to 87.8 Å^3/formula unit compared to those of the S_M and S_T phases, with volumes of 77.6 and 77.3 Å^3/formula unit, respectively. Using the following setting, i.e., $I4_1/amd$, $I4_1/a$, and $I2/b$ space groups for Z_T-, S_T-, and S_M-$BiVO_4$, respectively, it is possible to compare these three allotropes, with a common definition of the c-axis and the a−b plane. Such a setting will be used hereafter, allowing us to discuss optical anisotropy and excitonic spatial distribution using a common setting for the crystallographic directions for the $BiVO_4$ phases. Both scheelite (S_T and S_M) and zircon (Z_T) structures consist of isolated $[VO_4]^{3-}$ tetrahedra connected by $[BiO_8]^{5-}$ antiprisms but differ in the way these polyhedra are connected to each other. The structural phase transition between zircon and scheelite has been evidenced on the basis of a first-order reconstruction involving a "bond-switching" mechanism.[20] Panels a and b of Figure 1 show the consequences of such a structural filiation

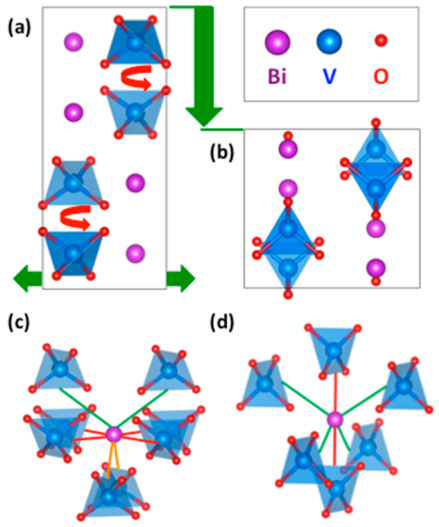

Figure 1. Schematic representation of the atomic structures of (a) S_M-$BiVO_4$ and (b) Z_T-$BiVO_4$. The structure filiation from S_M- to Z_T-$BiVO_4$ is highlighted with the green arrows (cell expansion along a and b, cell contraction along c) and the red arrows (rotation of VO_4^{3-} tetrahedra). The resulting local environments of bismuth atoms are given for (c) S_M-$BiVO_4$ and (d) Z_T-$BiVO_4$. A color code for the Bi−V bonds is used: red for the shortest, orange for intermediate, and green for the largest (see Table S1 for the related values).

between the S_M-$BiVO_4$ (or S_T) and Z_T-$BiVO_4$ phases. With the S_M phase as a starting point, three changes are observed to reach the Z_T phase: (1) a rotation of the $[VO_4]^{3-}$ tetrahedral units, (2) an expansion along the a- and b-axes of the monoclinic cell, and (3) a strong compression along the c-axis. The main impact of these structural modifications concerns the interconnection between the $[VO_4]^{3-}$ and $[BiO_8]^{5-}$ units as shown in panels c and d of Figure 1. The Bi−V bond lengths and Bi−O−V bond angles of S_M- and Z_T-$BiVO_4$ are summarized in Table S1 and will be discussed in more detail below, in the section devoted to optical anisotropy.

Before discussing our optical anisotropy results for these compounds, the properties of their excitons, and their potential impact on the related photocatalytic properties, we first validated our theoretical approach. To do so, we have compared the calculated energy-loss functions with the measured low-loss EELS spectra obtained from S_M- and Z_T-$BiVO_4$ samples. The DFT calculations have been performed by using two different codes, the Vienna Ab initio Simulation Package (VASP)[21] for the energy-loss functions, including LFE and the WIEN2k program package,[22] as a starting point for BSE evaluations of the excitonic properties. Most DFT calculations were performed with the Perdew, Burke, and Ernzerhof parametrization of the GGA (PBE-GGA) of the exchange-correlation potential.[23] BSE calculations were performed using a strategy similar to the one we used for the $CuAlO_2$ compound.[24]

Energy-Loss Function of S_M- and Z_T-$BiVO_4$. Electron energy-loss spectroscopy (EELS) measurements are directly related to the energy-loss function (ELF) defined by $\mathrm{Im}[-1/\varepsilon(\nu)] = \varepsilon_2(\nu)/[\varepsilon_1(\nu)^2 + \varepsilon_2(\nu)^2]$,where $\varepsilon_1(\nu)$ and $\varepsilon_2(\nu)$ are the

DOI: 10.1021/acs.chemmater.6b02261
Chem. Mater. 2017, 29, 3380−3386

real and imaginary parts of the dielectric function, respectively, where ν is the frequency.[25] Properly combined with first-principles calculations, it is an unrivaled tool for probing the frequency-dependent dielectric function over a high energy range.[26] The optical diffusion and absorption processes are directly related to $\varepsilon_1(\nu)$ and $\varepsilon_2(\nu)$, respectively. Figure 2 shows

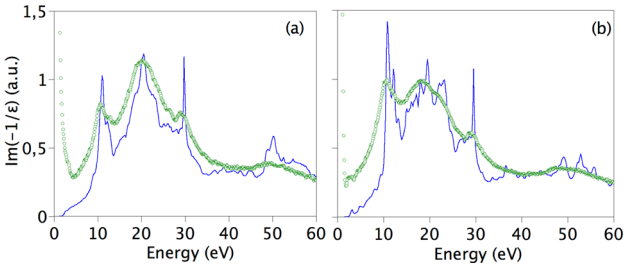

Figure 2. Energy-loss [$\mathrm{Im}(-1/\varepsilon)$] functions of (a) S_M-$BiVO_4$ and (b) Z_T-$BiVO_4$. The experimental VEELS spectra (empty green circles) of S_M- and Z_T-$BiVO_4$ have been recorded along the [9 11 4] and [1 1 0] zone axes, respectively. The calculated energy-loss and dielectric functions include local-field effects. For comparison, the calculated quantities correspond to an average of the polarizations along x, y, and z for S_M-$BiVO_4$ and a polarization along z for Z_T-$BiVO_4$.

the energy-loss function, $\mathrm{Im}(-1/\varepsilon)$, of S_M- and Z_T-$BiVO_4$. The experimental measurements have been performed with a small collection angle, allowing a direct comparison between the recorded and calculated loss functions at zero momentum transfer ($q \rightarrow 0$). Excellent agreement is obtained between these DFT calculations and orientation-dependent EELS measurements, as soon as the local-field effects (LFE) are taken into account in our simulations (more details on LFE are provided in the Supporting Information). In particular, the energy position and respective intensity of each spectral feature are well-reproduced. Such an agreement between PBE-GGA calculations and EELS measurements is not expected at first sight. Indeed, we expect an underestimation of the band gap value using PBE-GGA and thus a shift of all the simulated peaks with respect to the experimental spectrum. However, as previously reported,[26] PBE-GGA simulations give correct peak positions for the high-energy part of the spectrum ($E >$ 5 eV), while the band gap underestimation has a significant impact on the low-energy part of the spectrum ($E <$ 5 eV). We are in a similar situation except that no significant spectral feature can be detected at low energy, explaining such an overall agreement. In addition, it should be noted that PBE-GGA underestimates the band gap of $BiVO_4$ compounds by only 0.4 eV (see below).

We should mention that the loss functions are nearly the same along the three crystallographic directions for S_M-$BiVO_4$, in contrast to the case for Z_T-$BiVO_4$. This observation is important and allows us to consider an average loss function for S_M-$BiVO_4$, which makes the results independent of the orientation chosen during the experiments. In contrast, the comparison for Z_T-$BiVO_4$ requires a careful definition of the orientation axis (the origin of the different features is explained in Figure S2). It also should be noted that the tail of the zero-loss peak hinders the proper extraction of information below ~5 eV [the energy resolution of the microscope is around 0.8 eV (see the Supporting Information)]. As a consequence, the band gap offset and excitons cannot be probed with this experimental setup.

Optical Anisotropy in $BiVO_4$ and TiO_2. Using a standard DFT functional appears to be adequate for the description of the high-energy range of the dielectric function (from 5 to 60 eV). However, because band gaps are strongly underestimated in conventional DFT, a more advanced method is needed for an accurate description of the low-energy range (from 0 to 5 eV for instance). Consequently, we have used the Tran−Blaha modified Becke−Johnson (TB−mBJ) potential,[27] which is known for its ability to describe band gaps with an accuracy comparable to that of sophisticated GW calculations. In our DFT calculations, we have also taken into account relativistic effects on the valence electrons by including the spin−orbit (SO) coupling in our DFT calculations, to properly describe the Bi $p^{1/2}$ and Bi $p^{3/2}$ states, which are involved in the bands close to the Fermi level. Indeed, a band gap reduction of ~0.1 eV is observed when the SO coupling is switched on, for both S_M- and Z_T-$BiVO_4$.

Because in optical excitations the excited electron may interact with the hole it left behind, we had to go beyond standard DFT. By solving the two-particle BSE, one can properly describe the interaction between the electron and the hole of a photogenerated pair, i.e., the bound exciton state. Here, the starting point of the BSE calculations was not based on GW eigenvalues but on our GGA results with a band gap correction, which was defined in such a way to reproduce the TB−mBJ and GW band gaps of $BiVO_4$ and TiO_2, respectively. Such an approximation of the BSE spectra leads to results for TiO_2 similar to those starting from GW eigenvalues.[31]

From our DFT calculations (including SO coupling), we obtain an indirect and direct fundamental band gap for S_M- and Z_T-$BiVO_4$, which changes from 2.06 to 2.46 eV and from 2.47 to 2.84 eV for the two phases, respectively, when the TB potential mBJ is taken into account. This leads to a band gap correction of ~0.4 eV for the $BiVO_4$ compounds.

It should be noted that the indirect nature of the band gap of S_M-$BiVO_4$ has been recently experimentally confirmed,[28] with an energy difference between the indirect (2.56 eV) and direct (2.68 eV) band gaps of 0.12 eV, which agrees quite well with our prediction of 0.12 eV (2.47 and 2.59 eV for indirect and direct band gaps, respectively, for S_M-$BiVO_4$). In contrast, our calculations show a difference of 0.02 eV between the indirect (2.85 eV) and direct (2.87 eV) band gaps for Z_T-$BiVO_4$, which is not significant.

In panels a and b of Figure 3, the ε_2 function (in the low-energy range), deduced from BSE calculations, is plotted for S_M- and Z_T-$BiVO_4$, respectively. For comparison, we also show (in panels c and d of Figure 3) the ε_2 functions (based on BSE calculations) for anatase- and rutile-TiO_2, respectively. TiO_2 is the reference material in terms of photocatalytic performance in the UV range, while of the two phases of $BiVO_4$, one is a very promising candidate for photocatalysis in the visible range. In both cases, one phase (i.e., S_M-$BiVO_4$ and anatase-TiO_2) is known to have photocatalytic properties better than those of the other. Our idea is to compare these four systems and extract the main parameters that determine why only two of them is efficient in terms of photocatalytic activity, focusing on the optical absorption and exciton formation.

The in-plane (along the x-axis and/or y-axis) and out-of-plane (along the z-axis) contributions to the complex DF have been analyzed for the four aforementioned materials. The in-plane and out-of-plane notation refers to the 4-fold axis in Z_T-$BiVO_4$, anatase, and rutile, and the 2-fold axis in S_M-$BiVO_4$. Before discussing our predictions for $BiVO_4$, we consider the

DOI: 10.1021/acs.chemmater.6b02261
Chem. Mater. 2017, 29, 3380−3386

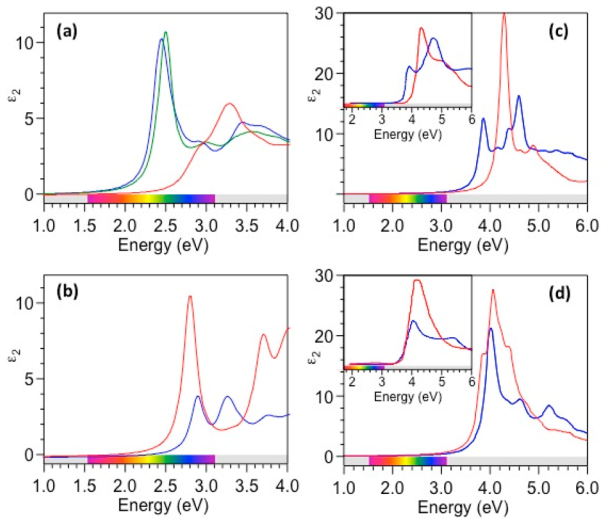

Figure 3. Imaginary part of the dielectric function for (a) S_M-$BiVO_4$, (b) Z_T-$BiVO_4$, (c) ana-TiO_2, and (d) rut-TiO_2 calculated via the BSE. The BSE-calculated spectra have been carefully converged for the energy range shown here (i.e., up to 4 and 6 eV for $BiVO_4$ and TiO_2, respectively). The *x*, *y*, and *z* polarizations are represented with blue, green, and red solid lines, respectively. Insets show the experimental spectra for anatase-TiO_2 and rutile-TiO_2.

two TiO_2 phases, for which experimental data are available (Figure 3c,d). The insets of panels c and d of Figure 3 provide the experimental ε_2 curves of the anatase and rutile TiO_2 phases, respectively, obtained at room temperature.[29] Very good agreement is obtained with the BSE calculations presented here. In particular, as previously demonstrated,[30,31] such BSE calculations can reproduce the anisotropic behavior of the optical properties of anatase and rutile TiO_2. The first optical excitations are from a polarization perpendicular versus parallel to the *c*-axis for anatase and rutile, respectively. In other words, anatase- and rutile-TiO_2 differ in their nature of the photoexcitations, where the former has two important polarizations (*x* and *y*) but the latter has only one (*z*).

The optical anisotropy for S_M-$BiVO_4$ (Figure 3a) is very strong in the low-energy range, in contrast to our previous observation for its related loss function in the high-energy range. The in-plane contribution leads to a band gap of ∼2.4 eV, instead of 2.9 eV for the out-of-plane contribution (see Table S1). Similarly, a strong anisotropy is found for Z_T-$BiVO_4$ (Figure 3b). However, the smallest optical gap is then observed for the out-of-plane contribution (2.8 eV), while the in-plane optical gap is ∼2.9 eV. In addition, the in-plane (out-of-plane) and out-of-plane (in-plane) excitations are quite intense (low) in S_M- and Z_T-$BiVO_4$. Such a difference between S_M- and Z_T-$BiVO_4$ is a direct consequence of the structural difference between these two phases, influencing the V−O and Bi−O interactions, which can easily be captured by the Bi−O−V bond angles and Bi−V distances (Table S1). Indeed, the reduction of the band gap from a pure binary oxide to the ternary $BiVO_4$ compounds is related to the presence of additional Bi−O and Bi−V interactions, which contribute to the anisotropy but in a different manner in the unit cell of S_M and Z_T. To be more specific, a bond angle of 90° and short Bi−V distances are preferred to yield an efficient 5p (Bi)−2p (O)−3d (V) interaction. These two criteria are satisfied only for the *x*−*y* plane in the S_M phase and along the *z*-axis in the Z_T phase. In summary, the optical anisotropy in S_M- and Z_T-$BiVO_4$ is very different at low energy, leading to an intense optical excitation in the visible range for a polarization perpendicular and parallel to the *c*-axis for S_M- and Z_T-$BiVO_4$, respectively. In other words, S_M-$BiVO_4$ and Z_T-$BiVO_4$ differ in their photoexcitations, which use two polarizations (*x* and *y*) in the former but one (*z*) in the later compound, respectively.

We cannot conclude at this stage that such a correlation between the anisotropy of the dielectric function and the photocatalytic performances does exist, but it is interesting to note that, in both TiO_2 and $BiVO_4$, the better photocatalytic phase is the one that shows an in-plane polarization. Additional aspects must be considered to explain the nearly zero photocatalytic activity of Z_T-$BiVO_4$ under visible light excitation, compared to S_M-$BiVO_4$. This difference could stem from the significantly larger band gap in the Z_T phase, which in our TB−mBJ calculations is ∼2.9 eV and thus on the very edge of energies that can be reached by visible light.

Excitonic Effects in $BiVO_4$ and TiO_2. An exciton is by definition a correlated electron−hole, bound by a Coulombic interaction. Figure 4 shows the first thousand excitons of the four systems and their energy distribution. Their binding energies (E_b) characterize their stability. A common feature is observed in the two photocatalytically active compounds, anatase-TiO_2 and S_M-$BiVO_4$. In both of these phases, the first exciton is bright and polarized perpendicularly with respect to the *c*-axis. This is in contrast to the inactive compounds rutile-TiO_2 and Z_T-$BiVO_4$, for which the first exciton is dark. In addition, the first bright exciton for rutile-TiO_2 is the 24th at 3.82 eV, with a polarization parallel to the *c*-axis and a strong binding energy of 605 meV.

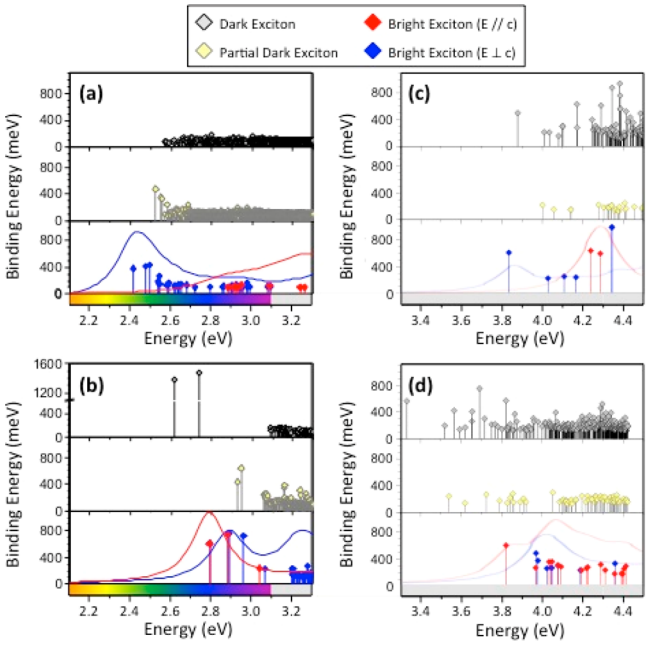

Figure 4. First excitons calculated via the BSE are shown as dark, partially dark, and bright (i.e., oscillator strength is zero, small, and large, respectively) for (a) S_M-$BiVO_4$, (b) Z_T-$BiVO_4$, (c) ana-TiO_2, and (d) rut-TiO_2. For each exciton, the binding energy is given. For the bright excitons, the imaginary part of the dielectric functions is given.

From the BSE calculations presented here, we can estimate the hole−electron weighted mean distance, hereafter $d_{h\text{-}e}$, which combined with E_b, the binding energy of the exciton, will be a measure of the probability of a hole−electron recombination,

DOI: 10.1021/acs.chemmater.6b02261
Chem. Mater. 2017, 29, 3380−3386

i.e., the exciton lifetime. $d_{h\text{-}e}$ has been estimated using the expression

$$\langle d_{\text{h-e}} \rangle = \frac{\sum_{h=1}^{N}\sum_{c=0}^{M}\sum_{e=1}^{N}(d_{h\text{-}e}^{c}P_{h\text{-}e}^{c})}{\sum_{h=1}^{N}\sum_{c=0}^{M}\sum_{e=1}^{N}P_{h\text{-}e}^{c}}$$

where $P_{h\text{-}e}^{c}$ is the probability of an hole−electron pair characterized by distance $d_{h\text{-}e}^{c}$ given by

$$P_{h\text{-}e}^{c} = \int_{r_h} \mathrm{d}^3 r_h \int_{r_e} \mathrm{d}^3 r_e W(r_h, r_e)$$

where $W(r_h,r_e)$ is the conditional probability of having an electron at r_e and a hole at r_h by

$$W(r_e, r_h) = \phi(r_e, r_h)\phi^*(r_e, r_h)$$

$\phi(r_e,r_h)$ and the BSE excitonic envelope function.

The three indices (h, c, and e) refer as to the position of the electron (e) and the hole (h) over the N atomic sites in the cell defined by the index c, where c ranges between 0 (origin cell) to M. M is taken such that the maximal h−e distance is ∼30 Å. The calculated probabilities for larger distances are negligible. In the calculations presented here, the hole is systematically in the cell at the origin (c = 0) and the bound electron in the cell c. A similar approach was used by Sharifzadeh et al.[32] to estimate the average h−e distance in organic solids.

Figure 5a shows a schematic representation of the way $\langle d_{h\text{-}e} \rangle$ is estimated. For the sake of simplicity, the unit cell contains only two atoms. The cell at the origin is highlighted in yellow; the orange lines represent the h−e contacts. Here the hole is defined on the oxygen site inside the cell at the origin and the promoted electron on a metal site. The h−e probabilities are proportional to the width of the lines; i.e., the thicker the lines, the larger the probabilities of creating an exciton between the two connected sites. By averaging all these weighted distances, we can thus define $\langle d_{h\text{-}e} \rangle$ based on the previous formula.

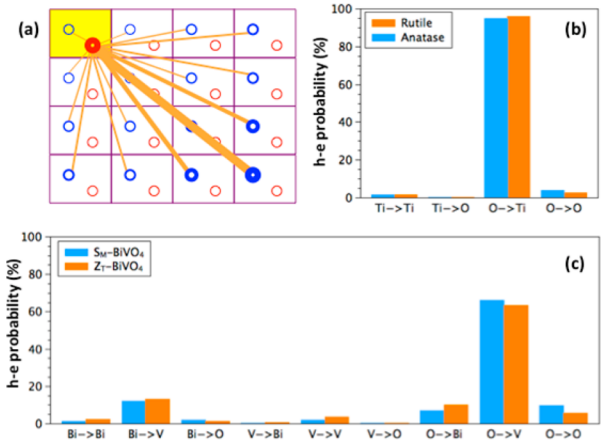

Figure 5. (a) Schematic representation of $\langle d_{h\text{-}e} \rangle$ for a unit cell containing only two atoms (oxygen in red, metal in blue). h−e probability distribution for (b) rutile- and anatase-TiO_2 and (c) S_M- and Z_T-$BiVO_4$. The photohole is inside the cell at the origin (defined by 000), and the photoelectron is distributed over all cells with a given h−e probability (proportional to the line width).

Panels b and c of Figure 5 show the distribution of the e−h probabilities for the first bright excitons of rutile-TiO_2, anatase-TiO_2, S_M-$BiVO_4$, and Z_T-$BiVO_4$. It clearly shows that in both rutile- and anatase-TiO_2, ∼95% of the excitons occur between oxygen and titanium atoms (the second largest $P_{e\text{-}h}$ is very small and corresponds to transitions between oxygen atoms due to hybridization effects). In $BiVO_4$, the main contribution to the exciton spectra originates from optical transitions between oxygen and vanadium (O → V, i.e., hole on O and electron on V) (66 and 63% of the transitions for S_M- and Z_T-$BiVO_4$, respectively), much more than the bismuth to vanadium transitions (with 12 and 13% relative weights for S_M- and Z_T-$BiVO_4$, respectively). Finally, O → Bi and O → O contributions are also observed but can be neglected. Moreover, while in TiO_2 the photohole was located nearly exclusively on oxygen, in $BiVO_4$ it is mainly positioned on oxygen but partly also on bismuth (>10%). Similarly, in TiO_2, the photoelectron is nearly exclusively located on the metal center (titanium). In contrast, in the vanadate ternary compounds, it is distributed on vanadium (slighty less than 80% with two transitions, O → V and Bi → V), bismuth (due to the O → Bi transition, with 7 and 10% in S_M- and Z_T-$BiVO_4$, respectively), and oxygen (due to the O → O transition, with 10 and 6% in S_M- and Z_T-$BiVO_4$, respectively). Such an excitonic distribution is a direct consequence of the orbital overlap in these compounds as illustrated in Figure S3 for Z_T-$BiVO_4$.

The optimal situation for avoiding electron−hole recombination is to have a small E_b and a large $d_{h\text{-}e}$. On the basis of the examination of average $d_{h\text{-}e}$ and E_b values, we plot in Figure 6

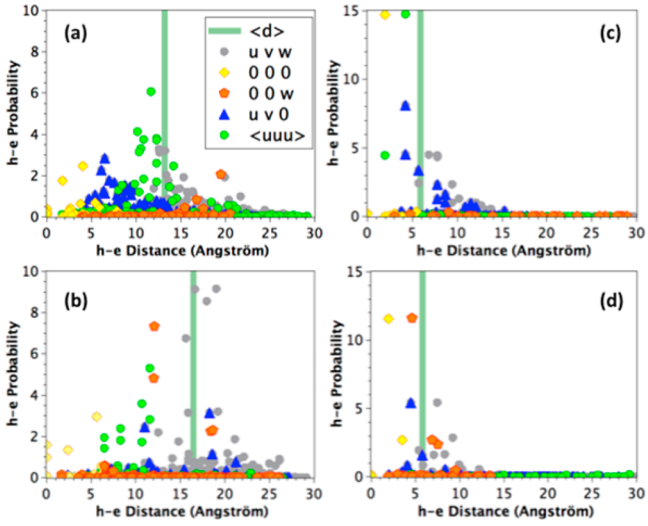

Figure 6. h−e distance distribution of the first bright excitons for (a) S_M-$BiVO_4$, (b) Z_T-$BiVO_4$, (c) ana-TiO_2, and (d) rut-TiO_2. It corresponds to excitons 1 (at 2.41 eV/E_b = 384 meV), 3 (at 2.79 eV/E_b = 610 meV), 1 (at 3.84 eV/E_b = 608 meV), and 24 (at 3.82 eV/E_b = 605 meV) for S_M-$BiVO_4$, Z_T-$BiVO_4$, anatase-TiO_2, and rutile-TiO_2, respectively. For each compound, the green bar highlights the mean h−e distance.

the probability that an electronic transition occurs versus its associated $d_{h\text{-}e}$ distance. Only the first bright excitons of the four compounds are taken into account. Among all the photoexcitations (represented with gray circles), some specific ones are highlighted. The ones corresponding to excitons localized in the unit cell are represented by yellow squares. The ones corresponding to an exciton that propagates in [uv0], [00w], and ⟨uuu⟩ directions are depicted by blue triangles, orange pentagons, and green circles, respectively. Finally, a green bar highlights the previously calculated average $d_{h\text{-}e}$ distance in each

DOI: 10.1021/acs.chemmater.6b02261
Chem. Mater. 2017, 29, 3380−3386

material for the given exciton. Note the similarities between S_M- and Z_T-$BiVO_4$, in terms of both the $d_{h\text{-}e}$ distance and the shape of the h−e distribution. In S_M-$BiVO_4$, Z_T-$BiVO_4$, and anatase-TiO_2, the excitons that propagate along ⟨*uuu*⟩ directions have high probabilities. In contrast, the highest probability in rutile-TiO_2 is found for excitons propagating along the [00*w*] direction. Figure 7 gives a very simple interpretation by

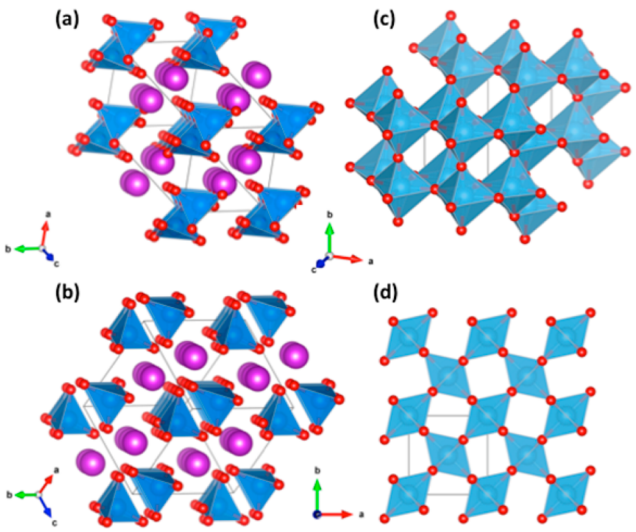

Figure 7. Projection of the atomic structure along the highest e−h probability direction for (a) S_M-$BiVO_4$, (b) Z_T-$BiVO_4$, (c) ana-TiO_2, and (d) rut-TiO_2. It corresponds to the ⟨111⟩ direction for panels a−c and the [001] direction for panel d.

showing the projection of the four structures along specific directions. Indeed, it appears that the exciton will propagate mainly in the direction of the highest packing of Bi in both $BiVO_4$ phases, which is along the ⟨*uuu*⟩ directions, and along the direction where the TiO_6 octahedra are sharing their edges, which is along ⟨*uuu*⟩ and [00*w*] directions for anatase- and rutile-TiO_2, respectively.

Another way to analyze our BSE data is to consider Tables S1−S4, which give the excitation energies, the oscillator strengths, and the binding energies of the principal bright excitons in the four systems. For instance, considering the first 50 excitons, 13 are bright in S_M-$BiVO_4$ but only 5 are bright in Z_T-$BiVO_4$. Similarly, among the first 50 excitons, 10 are bright in anatase-TiO_2 while only 1 is bright in rutile-TiO_2. In summary, under visible light excitation, more electron−hole pairs are formed in S_M-$BiVO_4$ than in Z_T-$BiVO_4$, and these excitons have the propensity to recombine more frequently in Z_T-$BiVO_4$ than in S_M-$BiVO_4$. A similar analysis could be done for anatase- and rutile-TiO_2.

CONCLUSION

In conclusion, this investigation reveals many common features between the reference UV light photocatalytic compound anatase-TiO_2 and the promising candidate for visible light photocatalytic compound S_M-$BiVO_4$. Indeed, both exhibit an indirect band gap, and their first exciton is bright and shows a polarization perpendicular to the *c*-axis. The fact that the band gap of the two photocatalytic active materials is indirect is essential in the sense that it prevents a direct recombination of the hole−electron pair, leading to a lifetime of photoexcited electrons and holes longer than that of direct band gap rutile-TiO_2 and Z_T-$BiVO_4$. In addition, the first excitons of these two last compounds are dark and show a polarization parallel to the *c*-axis. These inter-related properties appear to be essential and should be considered with care in the quest for an optimal photocatalytic material.

ASSOCIATED CONTENT

Supporting Information

The Supporting Information is available free of charge on the ACS Publications website at DOI: 10.1021/acs.chemmater.6b02261.

Details on the structural (Table S1), EELS (Figures S1−S2), densities of states (Figure S3) and BSE data (Tables S2−S5) are provided. Table S6 summarizes the main results in terms of optical and excitonic properties of S_M-, Z_T-$BiVO_4$, Anatase & Rutile TiO_2 (PDF)

AUTHOR INFORMATION

Corresponding Author

*E-mail: xavier.rocquefelte@univ-rennes1.fr.

ORCID

Xavier Rocquefelte: 0000-0003-0191-2354

Stéphane Jobic: 0000-0002-1900-0030

Author Contributions

X.R. and S.J. initiated the project. L.L. performed the EELS measurements and their analyses. T.D., P.B., and X.R. performed the DFT simulations. R.L. performed the BSE calculations. All authors analyzed the data, wrote the paper, and contributed to corrections and modifications.

Notes

The authors declare no competing financial interest.

ACKNOWLEDGMENTS

X.R. thanks T. Saison for the synthesis of S_M-$BiVO_4$ and Z_T-$BiVO_4$ and the CCIPL (Nantes) computing centre for computational facilities. P.B. was supported by the Austrian Science Foundation FWF (SFB F41 "Vicom"). L.L. acknowledges the support received from the European Union Seventh Framework Program under Grant Agreement 312483 ESTEEM2 (Integrated Infrastructure Initiative, I3) and from the European Union H2020 program under Grant 696656 Graphene Flagship.

REFERENCES

(1) Fujishima, A.; Honda, K. Electrochemical Photolysis of Water at a Semiconductor Electrode. *Nature* **1972**, *238*, 37−38.

(2) Walsh, A.; Yan, Y.; Huda; Al-Jassim, M. N.; Wei, S. − H. Band Edge Electronic Structure of $BiVO_4$: Elucidating the Role of the Bi s and V d Orbitals. *Chem. Mater.* **2009**, *21*, 547−551.

(3) Yeom, T. H.; Choh, S. H.; Song, K. J.; Jang, M. S. The domain structure of ferroelastic $BiVO_4$ studied by magnetic resonances. *J. Phys.: Condens. Matter* **1994**, *6*, 383−392.

(4) Yeom, T. H. The domain structure of ferroelastic $BiVO_4$ crystal studied by Gd^{3+} EPR. *Solid State Commun.* **2003**, *125*, 547−550.

(5) Manolikas, C.; Amelinckx, S. Ferroelastic domains in $BiVO_4$. *Phys. Status Solidi A* **1980**, *60*, 167−172.

(6) Kudo, A.; Omori, K.; Kato, H. A Novel Aqueous Process for Preparation of Crystal Form-Controlled and Highly Crystalline $BiVO_4$ Powder from layered Vanadates at Room Tempetarure and Its Photocatalytic and Photophysical Properties. *J. Am. Chem. Soc.* **1999**, *121*, 11459−11467.

DOI: 10.1021/acs.chemmater.6b02261
Chem. Mater. 2017, 29, 3380−3386

(7) Zhang, X.; Ai, Z.; Jia, F.; Zhang, L.; Fan, X.; Zou, Z. Selective synthesis and visible light photocatalytic activity of $BiVO_4$ with different crystalline phases. *Mater. Chem. Phys.* **2007**, *103*, 162−167.
(8) Li, C.; Pang, G.; Sun, S.; Feng, S. Phase transition of BiVO4 nanoparticles in molten salt and the enhancement of visible-light photocatalytic activity. *J. Nanopart. Res.* **2010**, *12*, 3069−3075.
(9) Tokunaga, S.; Kato, H.; Kudo, A. Selective Preparation of Monoclinic and Tetragonal $BiVO_4$ with Scheelite Structure and Their Photocatalytic Properties. *Chem. Mater.* **2001**, *13*, 4624−4628.
(10) Saison, T.; Chemin, N.; Chanéac, C.; Durupthy, O.; Mariey, L.; Maugé, F.; Brezova, V.; Jolivet, J. P. New Insights Into $BiVO_4$ Properties as Visible Light Photocatalyst. *J. Phys. Chem. C* **2015**, *119*, 12967.
(11) Fan, H.; Jiang, T.; Li, H.; Wang, D.; Wang, L.; Zhai, J.; He, D.; Wang, P.; Xie, T. Effect of $BiVO_4$ Crystalline Phases on the Photoinduced Carriers Behavior and Photocatalytic Activity. *J. Phys. Chem. C* **2012**, *116*, 2425−2430.
(12) Li, R.; Zhang, F.; Wang, D.; Yang, J.; Li, M.; Zhu, J.; Zhou, X.; Han, H.; Li, C. Spatial separation of photogenerated electrons and holes among {010} and {110} crystal facets of BiVO4. *Nat. Commun.* **2013**, *4*, 1432.
(13) Kweon, K. E.; Hwang, G. S. Hybrid density functional study of the structural, bonding, and electronic properties of bismuth vanadate. *Phys. Rev. B: Condens. Matter Mater. Phys.* **2012**, *86*, 165209.
(14) Zhao, Z.; Li, Z.; Zou, Z. Electronic structure and optical properties of monoclinic clinobisvanite $BiVO_4$. *Phys. Chem. Chem. Phys.* **2011**, *13*, 4746−4753.
(15) Wadnerkar, N.; English, N. J. Density theory functional investigations of bismuth vanadate: Effect of hybrid functionals. *Comput. Mater. Sci.* **2013**, *74*, 33−39.
(16) Aryasetiawan, F.; Gunnarsson, O.; Knupfer, M.; Fink, J. Local-field effects in NiO and Ni. *Phys. Rev. B: Condens. Matter Mater. Phys.* **1994**, *50*, 7311.
(17) Sham, L. J.; Rice, T. M. Many-Particle Derivation of the Effective-Mass Equation for the Wannier Exciton. *Phys. Rev.* **1966**, *144*, 708−714.
(18) Sleight, A. W.; Chen, H.-Y.; Ferretti, A.; Cox, D. E. Crystal growth and structure of BiVO4. *Mater. Res. Bull.* **1979**, *14*, 1571−1581.
(19) Dreyer, G.; Tillmanns, E. Dreyerite: ein naturliches, tetragonales wismutvanadat von Hirschhorn/Pfalz, NeuesJahrbuch fur Mineralogie, Monatshefte. 1981, Vol. *1981*, pp 151−154.
(20) Smirnov, M. B.; Mirgorodsky; Kazimirov, V. Yu.; Guinebretière, R. Bond-switching mechanism for the zircon-scheelite phase transition. *Phys. Rev. B: Condens. Matter Mater. Phys.* **2008**, *78*, 094109.
(21) Kresse, G.; Furthmuller, J. Efficient iterative schemes for ab-initio total-energy calculations using a plane-wave basis set. *Phys. Rev. B: Condens. Matter Mater. Phys.* **1996**, *54*, 11169.
(22) Blaha, P.; Schwarz, K.; Madsen, G. K. H.; Kvasnicka, D.; Luitz, J. *WIEN2k, An Augmented Plane Wave Plus Local Orbitals Program for Calculating Crystal Properties*; Vienna University of Technology: Vienna, 2001.
(23) Perdew, J. P.; Burke, K.; Ernzerhof, M. Generalized Gradient Approximation Made Simple. *Phys. Rev. Lett.* **1996**, *77*, 3865−3868.
(24) Laskowski, R.; Christensen, N. E.; Blaha, P.; Palanivel, B. Strong excitoniceffects in $CuAlO_2$ delafossite transparent conductive oxides. *Phys. Rev. B: Condens. Matter Mater. Phys.* **2009**, *79*, 165209.
(25) Ritchie, R. H. Plasma Losses by Fast Electrons in Thin Films. *Phys. Rev.* **1957**, *106*, 874.
(26) Lajaunie, L.; Boucher, F.; Dessapt, R.; Moreau, P. Strong anisotropic influence of local-field effects on the dielectric response α-MoO_3. *Phys. Rev. B: Condens. Matter Mater. Phys.* **2013**, *88*, 115141.
(27) Tran, F.; Blaha, P. Accurate Band Gaps of Semiconductors and Insulators with a Semilocal Exchange-Correlation Potential. *Phys. Rev. Lett.* **2009**, *102*, 226401.
(28) Cooper, J. K.; Gul, S.; Toma, F. M.; Chen, L.; Liu, Y. S.; Guo, J.; Ager, J. W.; Yano, J.; Sharp, I. D. Indirect Bandgap and Optical Properties of Monoclinic Bismuth Vanadate. *J. Phys. Chem. C* **2015**, *119*, 2969.
(29) Cardona, M.; Harbeke, G. Optical Properties and Band Structure of Wurtzite-Type Crystals and Rutile. *Phys. Rev.* **1965**, *137*, A1467.
(30) Kang, W.; Hybertsen, M. S. Quasiparticle and optical properties of rutile and anatase TiO_2. *Phys. Rev. B: Condens. Matter Mater. Phys.* **2010**, *82*, 085203.
(31) Chiodo, L.; Garcia-Lastra, J. M.; Iacomino, A.; Ossicini, S.; Zhao, J.; Petek, H.; Rubio, A. Self-energy and excitonic effects in the electronic and optical properties of TiO_2 crystalline phases. *Phys. Rev. B: Condens. Matter Mater. Phys.* **2010**, *82*, 045207.
(32) Sharifzadeh, S.; Darancet, P.; Kronik, L.; Neaton, J. B. Low-Energy Charge-Transfer Excitons in Organic Solids from First-Principles: The Case of Pentacene. *J. Phys. Chem. Lett.* **2013**, *4*, 2197−2201.

DOI: 10.1021/acs.chemmater.6b02261
Chem. Mater. 2017, 29, 3380−3386